# Anisotropic flat band and charge density wave in quasi-one-dimensional indium telluride

Meryem Bouaziz, Aymen Mahmoudi, Davide Romanin, Jean-Christophe Girard, Yannick J Dappe, François Bertran, Marco Pala, Julien Chaste, Fabrice Oehler, Abdelkarim Ouerghi

# Anisotropic flat band and charge density wave in quasi-one-dimensional indium telluride

Meryem Bouaziz,[1] Aymen Mahmoudi,[1] Davide Romanin,[1] Jean-Christophe Girard,[1] Yannick J. Dappe,[2] François Bertran,[3] Marco Pala,[4] Julien Chaste,[1] Fabrice Oehler,[1] and Abdelkarim Ouerghi[1,*]

[1]*Université Paris-Saclay, CNRS, Centre de Nanosciences et de Nanotechnologies, 91120, Palaiseau, Paris, France*

[2]*SPEC, CEA, CNRS, Université Paris-Saclay, CEA Saclay, Gif-sur-Yvette Cedex 91191, France*

[3]*Synchrotron SOLEIL, L'Orme des Merisiers, Départementale 128, 91190 Saint-Aubin, France*

[4]*DPIA, University of Udine, 33100 Udine, Italy*

(Received 12 March 2024; revised 12 June 2024; accepted 13 June 2024; published 25 July 2024)

Quasi-one-dimensional (quasi-1D) monochalcogenide compounds exhibit a strong in-plane anisotropy in their electronic band structure, which originates from their low crystallographic symmetry and provides an ideal platform for exploring collective electron behavior in confined systems. Here, we provide direct experimental evidence of electronic flat band near the Fermi level in quasi-1D InTe, using a combination of angle-resolved photoemission spectroscopy (ARPES), and density-functional theory (DFT). This flattened band extends about 0.4 $Å^{-1}$ one dimensionally in $k$-space area around the $M$ point according to ARPES and DFT. Using scanning tunneling microscopy, we found a modulation in the density of states along the $In^{1+}$ atoms, with a wavelength of two times the lattice constants. This periodic modulation order could be results from a Peierls instability, in which a spatial lattice distortion opens an electronic gap at the Fermi energy. Such quasi-1D InTe crystals provide a platform for fundamental research and future applications which relies on collective electronic behavior of a quasi-1D semiconductor.

DOI: 10.1103/PhysRevB.110.045441

Low-dimensional electronic systems have been found to host a great variety of physics [1]. In the context of bidimensional materials [2–4] van der Waals heterostructures [5–7] and topological surface states of strong topological insulators have already been investigated [8,9]. Further lowering the dimensionality, e.g., from bidimensional (2D) [10] to quasi-one-dimensional (quasi-1D) [11,12] can result in fascinating phenomena, such as topological edge states [9] or one-dimensional (1D) charge-density waves (CDW) [13]. For this last class of phenomena, the charge ordering can be induced in one dimension by a periodic spatial distortion of the crystal structure, which is referred to as Peierls ordering transition [1,14,11]. Peierls-related effects are often induced in solids by strong Coulomb repulsion between carriers [13], for which the low-dimensionality character [15,16] further enhances the electronic confinement.

A Peierls transition corresponds to a distortion of the atomic positions together with an associated metal-to-insulator phase transition at a certain critical temperature $T_{CDW}$, when lowering the temperature from an undistorted high-temperature phase to a low-temperature phase. Such Peierls transitions have already been observed in their simplest form as CDW distortions in carbyne [17] or aromatic molecules [16]. Many other quasi-1D dimensional systems exhibit CDW variants [18], such as $In_2Se_3$ [19,20], CuTe [15], conducting polymers, quasi-one-dimensional metals [19], or self-assembled atomic chains adsorbed on semiconducting surfaces [21]. In the case of InTe, the crystal already shows a highly anisotropic character of the electronic band structure and optical properties [22]. This has motivated thermal transport studies, which have revealed a high Seebeck effect in InTe [23,24] with potential application in high-efficiency thermoelectric devices [25]. The InTe crystal structure can be described as infinite chains of covalently bonded $(InTe_2)^-$ polyhedra along the $c$ direction, intercalated by mobile $In^{1+}$ atoms along the $a$- and $b$ directions [26,27]. This strong anisotropy in the crystal structure leads to quasi-1D features in the phonon and electronic band dispersions, which can be isolated by their specific micro-Raman response from the respective in-plane lattice vibrations [22], or by several optical polarization properties due to anisotropic electron-hole excitations [28]. In a recent study, we have identified $In^{1+}$ vacancies at the (110) surface of InTe and demonstrated their relation to the strong $p$-type character [22,29]. These mobile $In^{1+}$ atoms at the cleaved (110) surface are also responsible for the strong ionic character of the cohesion forces between the static quasi-1D array of covalent $(InTe_2)^-$ chains. It is interesting to compare the electronic properties of InTe with that of ionic crystals, such as $In_4Se_3$ [19,30,12]. As a matter of fact, there is some similarity between InTe and the cleavable $In_4Se_3$, in a sense that in both structures, the covalently bonded layers are separated by layers of $In^+$ cations [25,26].

Here, we report the electronic properties of quasi-1D InTe using angle-resolved photoemission spectroscopy (ARPES) and scanning tunnel microscopy/spectroscopy (STM/STS) on a UHV-cleaved surface. We reveal the existence of a stable distortion of the ionic surface with interesting electronic properties that could broaden the scope of 2D and quasi-1D materials. The ARPES measurement shows that InTe exhibits

*Contact author: abdelkarim.ouerghi@c2n.upsaclay.fr

 

a highly flat band along $\overline{ZMZ}$ direction near the Fermi energy $E_F$. Those bands provide a large effective mass close to the Fermi level leading to a large density of state (DOS). Using STS, we obtain a detailed picture of the charge redistribution within two times the lattice constants of InTe. The coexisting apparent atomically resolved periodic and energy gap clearly shows a Peierls-type CDW. Our results demonstrate that InTe is an intrinsic quasi-1D with the presence of a flat band, which marks a significant step toward the studies of electronic properties of quasi-1D materials.

InTe adopts a conventional (nonprimitive) tetragonal unit cell described by space group *I*4/*mcm*, which can be better represented by the chemical formula of $(In^{1+})$ $(In^{3+}Te_2^{2-})$. Figure 1(a) shows the projected structure of InTe along the [110] axis. The tetragonal crystal has the same lattice constant $a = 8.44$ Å along the [100] and [010] directions and shows a shorter $c = 7.13$ Å along the [001]. The $In^{3+}$ and $In^{1+}$ atoms occupy two different crystallographic positions with different chemical bonding environments. Each $In^{3+}$ cation is tetrahedrally coordinated to four $Te^{2-}$ anions, thus exhibiting a covalent $In^{3+}Te_4^{2-}$ substructure. The remaining $In^{+}$ cations display a distorted square antiprismatic coordination with eight surrounding $Te^{2-}$ ions. These $In^{+}$ cations are linked to the covalent $(In^{3+}Te_4^{2-})$ units by weak electrostatic interactions, which gives rise to their quasi one-dimensional electronic properties [26,22]. Due to the weaker bond strengths between neighboring $(In^{3+}Te_4^{2-})$ chain, the (110) plane becomes a natural cleavage. As shown in Fig. 1(a), the (110) surface of bulk InTe exhibits a rectangular symmetry with parameter $a\sqrt{2}$ and $c$ (black rectangle). The positions of the exposed $In^{1+}$ atoms are described by a smaller rectangular lattice, with half the size of the surface cell in both in-plane directions: $(a\sqrt{2})/2$ and $c/2$ [red rectangle in Fig. 1(a)]. In Fig. 1(b), we report the electronic structure of bulk InTe, as calculated from the Heyd-Scuseria-Ernzerhof (HSE) hybrid functionals [22]. Due to the crystal symmetry, the $\Gamma X$ direction in reciprocal space coincides with the normal of the (110) plane in real space. The corresponding slice of the 3D Brillouin zone (BZ) is shown in the inset, with the $\overline{ZMZ}$ direction along [001] in the real space. The minimum of the conduction band appears in the interval between $\bar{X}$ and $\bar{P}$ points. Instead, the valence-band maximum (VBM) is well determined at the $\bar{M}$ point. Most interestingly, the electronic structure is arranged in a peculiar way near the $\bar{M}$ point, with an extended flat dispersion region of both the conduction-band minimum (CBM) and the VBM around the BZ. In VBM, the flat dispersion almost extends to the $\bar{Z}$ valley, but the $\bar{M}$ valley has still higher energy than the VBM at $\bar{Z}$. Moreover, the CBM is mostly flat, but CBM at the $\bar{Z}$ valley is slightly lower in energy than the local minima at $\bar{M}$. The most striking feature of the band structure is its strong anisotropy at $\bar{M}$, as the extended flat dispersion at $\bar{M}$ along the $\overline{ZMZ}$ direction ($\sim$0.4 Å$^{-1}$) is completely missing along the perpendicular $\overline{XMX}$ direction. The strong anisotropy of the InTe band structure suggests its consideration as a quasi-1D system. Figure 1(b) further shows the calculated DOS of the bulk InTe, in which we can see a very sharp peak at the top of the valence band. This peculiar electronic feature results from the nondispersive character of the top of the valence band and the low dispersion at the bottom of the conduction band.

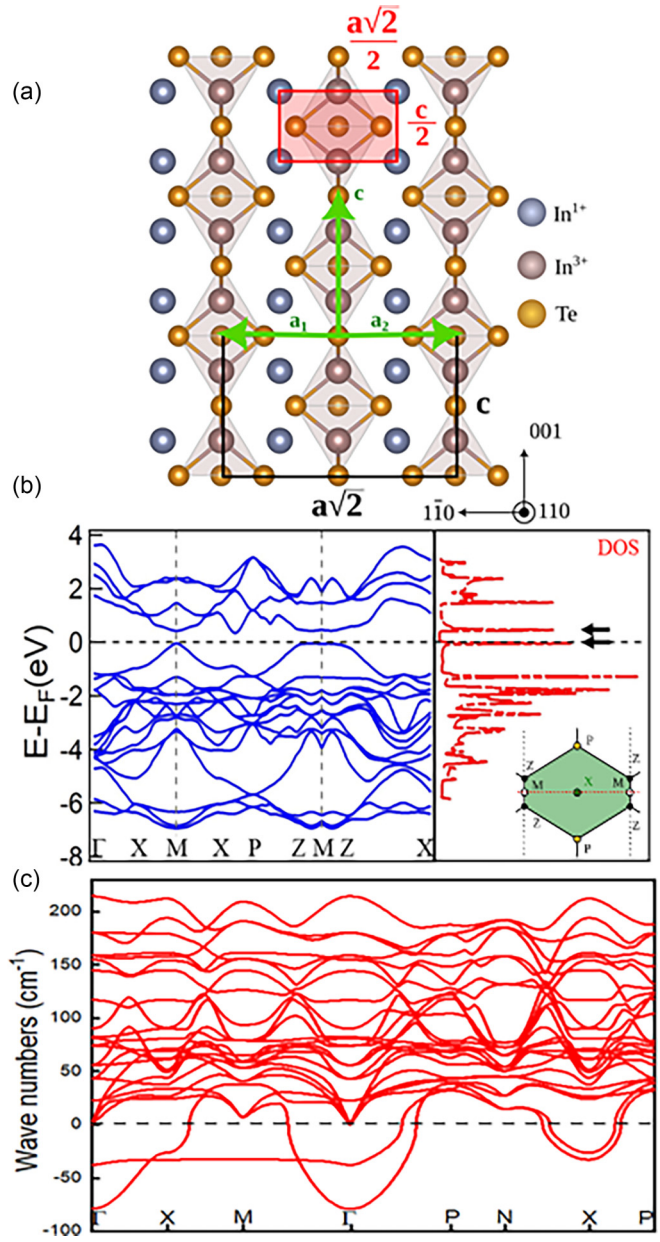


FIG. 1. Structural and electronic properties of InTe: (a) Crystal structure of tetragonal InTe. The black rectangle shows, respectively, the bulk at tellurium atoms and the red rectangle unit cell for the surface-topmost $In^{1+}$, (b) The band structure of InTe obtained from a DFT-HSE calculations, (c) Phonon dispersion of InTe calculated at relaxed lattice constant via the PBESOL0 functional reveals a flat branch containing modes of imaginary frequencies at the $X$ point along $\Gamma$-$X$-$M$-$\Gamma$ directions.

Figure 1(c) shows the phonon band-structure calculations of InTe, performed by density-functional theory (DFT) calculation. We find significant instabilities near $X$ points and $\Gamma-X-M$ direction below the dashed black line in Fig. 1(c), as also confirmed by others in precedent published studies [25,27]. It is reported that the unstable phonon spectrum comes from the $5s^2$ pair electron around $In^{1+}$ atoms [25]. The presence of such negative frequencies in the phonon dispersion is a signature of dynamical instabilities [31]. In our case,

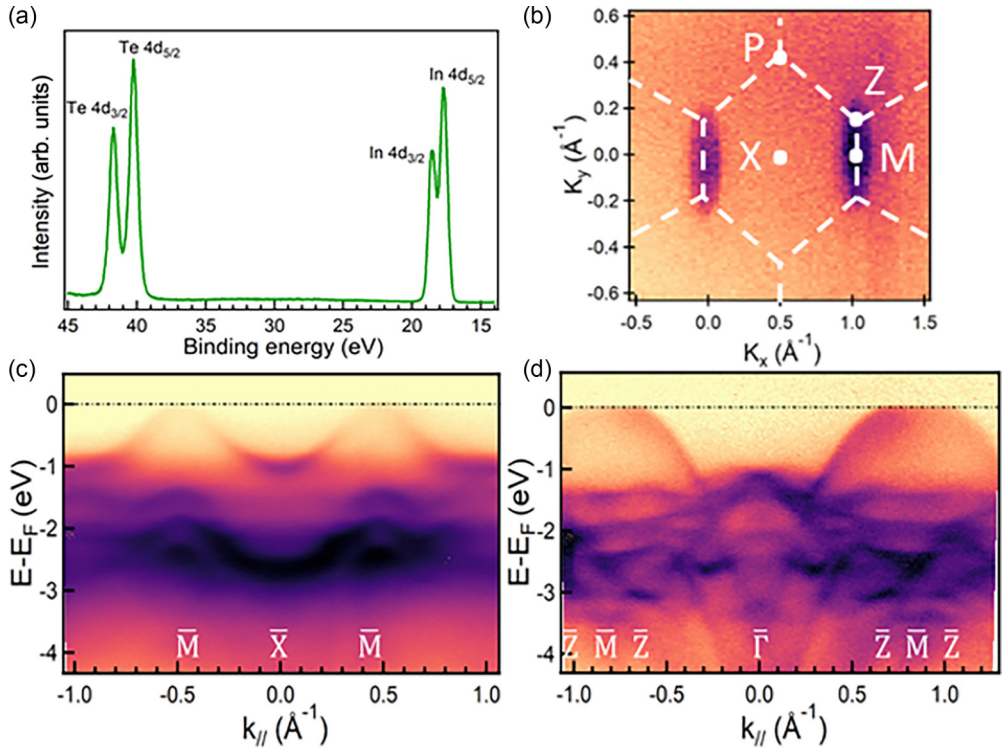


FIG. 2. (a) High-resolution XPS spectra of Te 4*d* and In 4*d* core levels, (b) Constant ARPES energy surfaces for InTe ($h\nu = 50$ eV) taken at $E_F$, white lines correspond to the 2D BZ obtained using the in-plane cell parameter of InTe, (c), (d) Electronic structure measured by ARPES at a photon energy of 84 eV.

the instability occurs at the *X* and *M* points in reciprocal space of the bulk InTe unit cell.

To experimentally resolve the electronic band-structure properties of InTe, we performed x-ray photoemission spectroscopy (XPS)/ARPES measurements. Our sample is a commercial InTe crystal from 2D semiconductors. XPS measurements confirm the expected stoichiometry of In and Te in the crystal [Fig. 2(a)]. The spectrum reveals no oxide or oxygen-related spectroscopic features, for both In and Te components. In Fig. 2(b), we have superimposed the projected 2D BZ of tetragonal InTe for the (110) surface on the Fermi surface in the $\overline{XMP}$ plane at 50 eV. The isoenergetic contours exhibit a marked elliptical symmetry at the $\bar{M}$ point, which is the direct electronic consequence of the highly anisotropic structure of the bulk (undistorted) InTe unit cell. This was explained in a previous study by the dominant native defects formed by $In^{1+}$ vacancies [29]. In Figs. 2(c) and 2(d), more insight into the InTe electronic structure was obtained along two projected high-symmetry lines, $\overline{MXM}$ and $\overline{ZMZ}$, measured at 84 eV. As expected, the measured ARPES projection along $\overline{ZMZ}$ is completely different from that measured perpendicularly, along $\overline{MXM}$. This figures demonstrate the high anisotropy and the lower dispersion-shaped energy near the Fermi level as a typical signature of quasi-1D band structure of InTe [26].

To further investigate this anisotropy distribution of the flat band, in Figs. 3(a) and 3(b), we report the InTe band-structure projection at 50 eV. The intensity of the band near the $E_F$ is sharp and lower dispersive. These features are further displayed in the momentum distribution curves (MDCs) [Figs. 3(c) and 3(d)]. From the analysis of the MDC, we confirm a high density of states at the Fermi level, in agreement with the predicted DFT calculations [Fig. 1(b)]. The band around $\bar{M}$ extends about $\sim 0.01$ Å$^{-1}$ along $\overline{MXM}$ and is larger along $\overline{ZMZ}$ ($\sim 0.4$ Å$^{-1}$), with a down dispersion toward $\bar{Z}$ and $\bar{X}$. It is noteworthy that this sample is highly *p* doped and the VBM is located close to the $E_F$.

In Figs. 3(e) and 3(f), we superpose the theoretical DFT dispersions along $\overline{ZMZ}$ and $\overline{MXM}$. All main features are well reproduced by the calculated band structures for both directions. The electronic band structure is dispersive along the $\overline{MX}$ direction and nearly flat along the $\overline{MZ}$ direction. Near the $\overline{M}$ point of the bulk Brillouin zone, the quasi-1D band is mainly formed by *p* orbitals of Te with small contribution of $In^{1+}$ *s* orbitals. At the excitation photon energy of 50 eV, the photoionization cross section of these orbitals is similar, supporting that InTe ARPES signal is dominated by Te *p* orbitals. We thus derive two experimental values of effective masses for the holes at the $\bar{M}$ point by fitting the curves along the $\overline{MX}$ and $\overline{MZ}$ directions. We obtain 0.2 $m_0$ ($m_0$ is the free-electron mass) for the first while it tends towards infinity along the flat band. This result proves that InTe conduction occurs along only one direction of the crystallographic coordinate, making InTe a quasi-1D material [32].

STM/STS imaging of the InTe surface is the most direct way to investigate the electronic properties of InTe [13]. High-resolution STM images show the atomic structure of InTe (110) acquired at room temperature [Fig. 4(a)] and at 77 K, where two regions are clearly distinguishable: defect-free area [Fig. 4(b)] and defective zone [Fig. 4(c)]. We observe

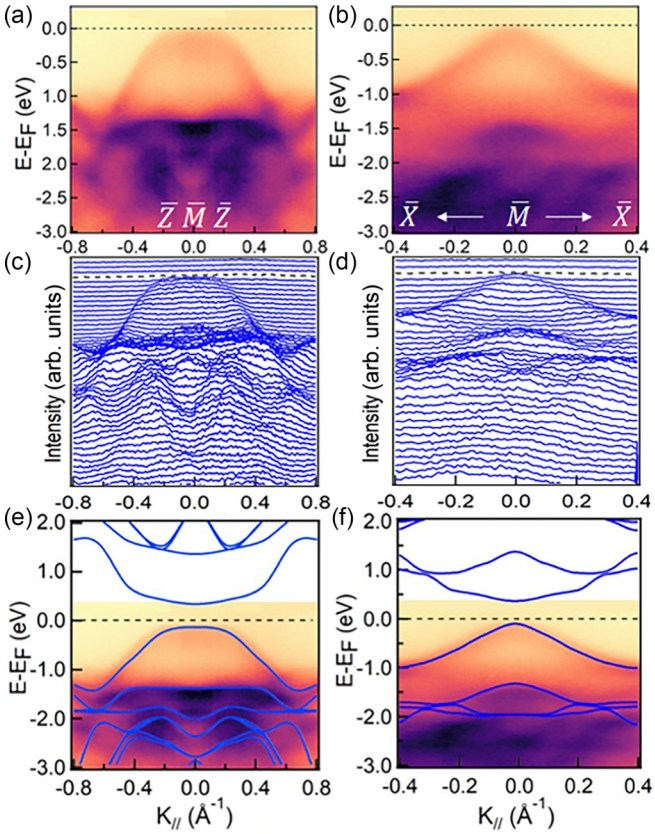


FIG. 3. Energy vs momentum dispersion of InTe at photon energy $h\nu = 50$ eV along $\overline{ZMZ}$ and $\overline{XMX}$, respectively**:** (a), (b) ARPES energy distribution curves of InTe showing the presence of a flat band near the $E_F$ in the $\overline{MZ}$ direction, (c), (d) Corresponding MDCs of InTe, respectively. (e), (f) Same ARPES data with superposed band structure from DFT calculation of InTe.

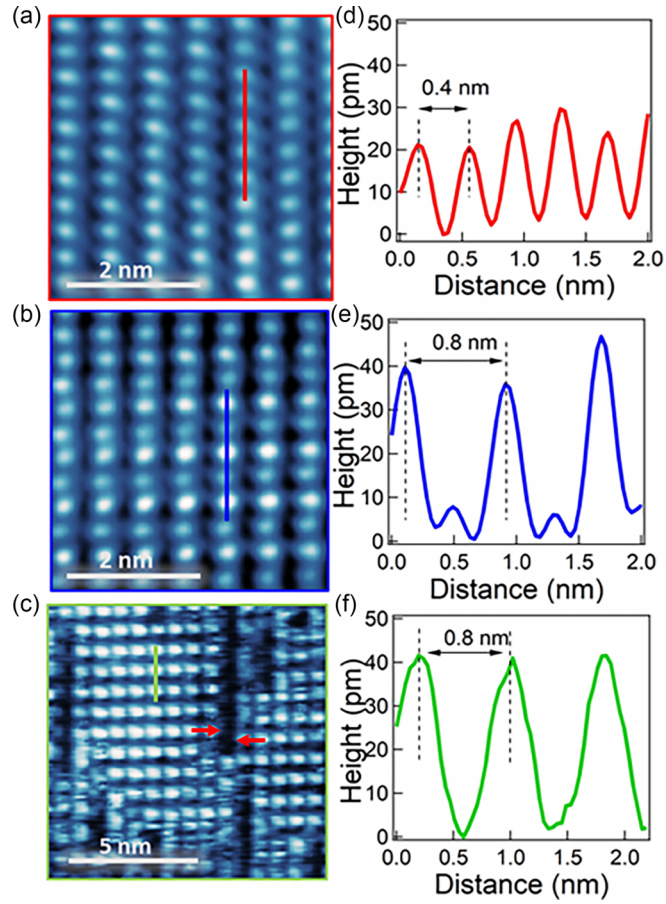


FIG. 4. STM images of InTe (110) UHV-cleaved surface. (a) Room-temperature measurement ($U = 0.2$ V, $I = 100$ pA) with spatial periodicity of $c/2$ along the $In^{1+}$ atoms. (b) Image measured at 77 K in nondefective area with a modulation wavelength of $2 \times c/2$ ($U = 0.2$ V, $I = 100$ pA). (c) Image measured at 77 K with $In^{+}$ defect lines showing a periodicity of the CDW about ~0.8 nm ($U = -0.5$ V, $I = 30$ pA). (d), (e), and (f) are the profile lines corresponding to (a), (b), and (c), respectively.

sharply defined chains, all aligned along the in-plane $c$ direction. These bright lines have previously been described as $In^{1+}$ atom chains [29]. The apparent height of these features depends strongly on the bias applied between the tip and sample, showing that the STM contrast originates from the locally modified electronic structure rather than from topographic features. The three images share the same periodicity of $a\sqrt{2}/2$ along the direction perpendicular to the $c$-axis chain direction. In contrast, the structure of each chain is different along the $c$ axis.

To quantify these differences, more details are described in Figs. 4(d), 4(e), and 4(f) with the corresponding line profiles, extracted from the positions marked in red, blue, and green lines. In Fig. 4(a), we measure a spatial periodicity of $c/2$ (~0.4 nm) along the $In^{1+}$ atoms, confirmed by the corresponding line profile in red. This is coherent with the lattice parameters of the (110) surface [Fig. 1(a)]. At low temperature (77 K), Fig. 4(b) shows a contrast effect between lines as the intensity of the spots alternates between brighter and less sharp in the defect-free area. This contrast is supported by a modulation of the electronic states with a wavelength of $c$ (~0.8 nm) explained by the profile line in blue. The contrast modulation contrasts with conventional surface reconstructions observed in semiconductors, which require the dimerization or removal of atoms to fulfill local charge states and minimize the number of broken bonds. The result agrees with STM study of CDW on the $NbSe_2$, proving that STM difference intensity is due to CDW signal [33]. The full transition structure is presented in Fig. 4(c). The modulation of the lattice structure is reflected in the height profile along the $In^{1+}$ chains with an average modulation period of $0.8 \pm 0.05$ nm, equivalent to two times the lattice constants [Fig. 4(f)]. This figure shows that our InTe sample contains several indium chain defects. It should be specified that the size of the structure is about 5 nm × 5 nm and the spatial modulations of the $In^{1+}$ chains are misaligned between different areas, forming an inhomogeneous pattern at the large scale. This may explain the transition compared to Fig. 4(b), which are imaged in a free-defect area. Finally, the difference of STM intensity between Figs. 4(a) and 4(c) could be explained as a modulation of charge density associated with a transition to the low-symmetry structure as observed by STM for low-temperature CWD in the 1D $MoSe_2$ [14].

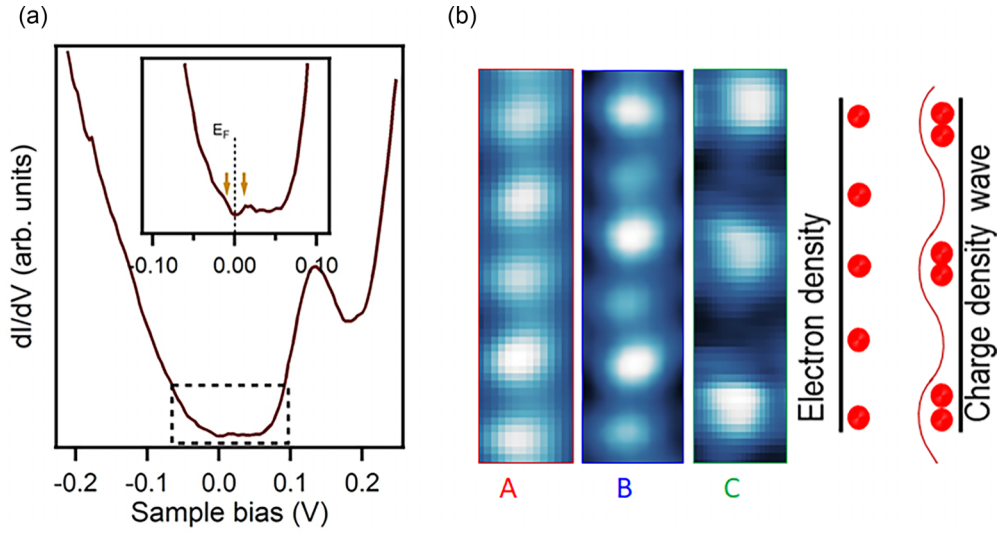


FIG. 5. (a) The *dI/dV* spectrum as a function of the bias voltage, showing that the energy band gap is about ∼20 meV, (b) The schematic illustrates the relationship between the three modulations in Fig. 4.

To confirm the link between spatial ordering modulation, we measured the InTe LDOS using *dI/dV* spectroscopy within the area shown in Fig. 4(c). Figure 5(a) shows a *dI/dV* spectrum from cleaved InTe within the semiconducting band gap [29]. The VBM is located at 10 meV below the Fermi level. A high-resolution view of this spectrum around $E_F$ [inset in Fig. 5(a)] revealed an energy gap of 20 meV with two peaks at the band edges. Statistical analysis of ten different InTe regions at $T = 77$ K yields an average gap size of $20 \pm 5$ meV. The modulation of STM intensity and the presence of a band gap at the Femi level are best explained by Peierls-type charge-density wave order intrinsic to InTe [1,13,11]. The CDW in InTe gives rise to a doubling of the periodicity, as can be seen in the low-temperature STM images shown in Figs. 4(b) and 4(c). The real-space periodicity of the CDW is schematically shown in Fig. 5(b).

In the main, our STM measurements demonstrated that electronic properties can be strongly affected by intrinsic defects [Fig. 4(c)]. It is thus the key parameter that induces the modification of InTe electronic properties. It is worth noting that the lateral size of the observed structure is lower than 5 nm × 5 nm, predominantly presented in STM images [Fig. 4(c)] and much smaller than the conventional ARPES beam size (50 - 50 μm) [34,35]. In addition, the small domains are misaligned and form inhomogeneous patterns, as shown by the red arrows between the line defects [36]. Our STM results demonstrate that the CDW in InTe exist on a very small area and can be quenched or suppressed at large scale [20]. In this respect, the observation of short-range phase-coherent CDW small domains in InTe can explain the absence of a band-gap opening in the electronic band dispersions at large scale. To further study the CDW effect on InTe, one should measure the transport properties (as a function of temperature) and the calculation of the electronic susceptibility.

In conclusion, the band structures of InTe are investigated both from the experimental and theoretical perspectives. ARPES measurements reveal that electronic flat bands near the $\bar{M}$ point have an extension of about 0.4 $Å^{-1}$. The quasi-1D crystal structure of InTe consisting of $In^{1+}$ ions chains is consistent with the Peierls-type CDW, fully characterized by combined STM/STS measurement. Hence, we found a periodic modulation in the density of states along the $In^{1+}$ ions chains, with a wavelength of 2 lattice constants. The coexistences of Peierls-type CDW, and lattice anharmonicity with large flat band in InTe are the origin of the intriguing physical properties of the compounds. Our findings provide guidance to understanding the underlying mechanism of quasi-1D electronic transport in InTe and further improving the performance of electronic and optoelectronic devices based on layered anisotropic semiconductors.

The datasets generated during and/or analyzed during the current study are available from the corresponding author on reasonable request.

## ACKNOWLEDGMENTS

We acknowledge the financial support by DEEP2D (Grant No. ANR-22-CE09-0013), 2D-on-Demand (Grant ANR-20-CE09-0026), MixDferro (Grant No. ANR-21-CE09-0029), TyLDE (Grant No. ANR-23-CE50- 0001-01), ADICT (Grant No. ANR-22-PEEL-0011), and FastNano (Grant No. ANR-22-PEXD-0006) projects, as well as the French technological network RENATECH. D.R. acknowledges support from the HPC resources of IDRIS, CINES, and TGCC under Allocation No. 2023-A0140914101 made by GENCI.

## APPENDIX

### 1. Photoemission spectroscopy

ARPES experiments were performed at the CASSIOPEE beamline of the SOLEIL synchrotron light source. The CASSIOPEE beamline is equipped with a Scienta R4000 hemispherical electron analyzer whose angular acceptance is ±15° (Scienta Wide Angle Lens). The valence-band data were calibrated with respect to the Fermi level. High-quality samples from the "2D semiconductors" company were cleaved in UHV at a base pressure better than $1 \times 10^{-10}$ mbar [37]. The Fermi level was determined by fitting the leading edge

of the gold crystal at the same photon energies and under the same experimental conditions. The experiment was performed at $T = 30$ K. The incident photon beam was focused into a 50-μm spot (in diameter) on the sample surface. All ARPES measurements were performed with a linear horizontal polarization [22].

### 2. Scanning tunneling microscopy

STM experiments were performed at 77 K using an LT-STM (Scienta-Omicron). The sample was prepared in the same conditions compared to ARPES measurements, cleaved at a base pressure better than $1 \times 10^{-10}$ mbar, and transferred immediately in the precooled STM head. STM images were acquired in the constant-current mode.

### 3. *Ab initio* phonon calculations

Vibrational properties were obtained via localized Gaussian basis functions and the PBESOL0 hybrid functional as implemented in the CRYSTAL23 code [38]. We used the triple-polarized Gaussian-type basis set [39] with real-space integration tolerances of 10–10–10–25–50 and a total energy tolerance of $10^{-10}$ Ha. The Brillouin zone was uniformly sampled with a grid of $24 \times 24 \times 24\,k$ points when calculating the electronic properties of the unit cell. Phonon calculations were obtained, after relaxation of the cell and atoms' positions, via the finite-displacement method as implemented in CRYSTAL23 [40], where force constants were calculated in a $2 \times 2 \times 2$ supercell and $k$-point sampling were reduced accordingly.


[1] Y. Xia, J. Zhang, Y. Jin, W. Ho, H. Xu, and M. Xie, Charge density modulation and the Luttinger liquid sin $MoSe_2$ mirror twin boundaries, ACS Nano **14**, 10716 (2020).

[2] D. A. Bandurin *et al.*, High electron mobility, quantum Hall effect and anomalous optical response in atomically thin InSe, Nat. Nanotechnol. **12**, 223 (2017).

[3] D. Jariwala, T. J. Marks, and M. C. Hersam, Mixed-dimensional van der Waals heterostructures, Nat. Mater. **16**, 170 (2016).

[4] Z. Ben Aziza *et al.*, Tunable quasiparticle band gap in few-layer GaSe /graphene van der Waals heterostructures, Phys. Rev. B **96**, 035407 (2017).

[5] T. Georgiou *et al.*, Vertical field-effect transistor based on graphene-$WS_2$ heterostructures for flexible and transparent electronics, Nat. Nanotechnol. **8**, 100 (2012).

[6] C.-H. Lee *et al.*, Atomically thin p–n junctions with van der Waals heterointerfaces, Nat. Nanotechnol. **9**, 676 (2014).

[7] P. Gehring, B. F. Gao, M. Burghard, and K. Kern, Growth of high-mobility $Bi_2Te_2Se$ nanoplatelets on hBN sheets by van der Waals epitaxy, Nano Lett. **12**, 5137 (2012).

[8] M. Bianchi *et al.*, Coexistence of the topological state and a two-dimensional electron gas on the surface of $Bi_2Se_3$, Nat. Commun. **1**, 128 (2010).

[9] J. Seo *et al.*, Transmission of topological surface states through surface barriers, Nature (London) **466**, 343 (2010).

[10] L. Britnell *et al.*, Strong light-matter interactions in heterostructures of atomically thin films, Science **340**, 1311 (2013).

[11] S. Barja *et al.*, Charge density wave order in 1D mirror twin boundaries of single-layer $MoSe_2$, Nat. Phys. **12**, 751 (2016).

[12] N. S. Vorobeva *et al.*, Anisotropic properties of quasi-1D $In_4Se_3$: Mechanical exfoliation, electronic transport, and polarization-dependent photoresponse, Adv. Funct. Mater. **31**, 2106459 (2021).

[13] L. Wang *et al.*, Direct observation of one-dimensional Peierls-type charge density wave in twin boundaries of monolayer $MoSe_2$, ACS Nano **14**, 8299 (2020).

[14] Y. Ma *et al.*, Angle resolved photoemission spectroscopy reveals spin charge separation in metallic $MoSe_2$ grain boundary, Nat. Commun. **8**, 14231 (2017).

[15] M. Campetella, G. Marini, J. S. Zhou, and M. Calandra, Electron-phonon driven charge density wave in CuTe, Phys. Rev. B **108**, 024304 (2023).

[16] D. Romanin *et al.*, Dominant role of quantum anharmonicity in the stability and optical properties of infinite linear acetylenic carbon chains, J. Phys. Chem. Lett. **12**, 10339 (2021).

[17] D. Romanin and M. Calandra, Giant quantum anharmonic effects on the stability, vibrational and optical properties of cyclo[4n+2]carbon, Carbon Trends **9**, 100207 (2022).

[18] Z. Z. Wang, J. C. Girard, C. Pasquier, D. Jérome, and K. Bechgaard, Scanning tunneling microscopy in TTF-TCNQ: Phase and amplitude modulated charge density waves, Phys. Rev. B **67**, 121401 (2003).

[19] J. S. Rhyee *et al.*, Peierls distortion as a route to high thermoelectric performance in $In_4Se_3$ crystals, Nature (London) **459**, 965 (2009).

[20] M. Hoesch *et al.*, Disorder quenching of the charge density wave in $ZrTe_3$, Phys. Rev. Lett. **122**, 017601 (2019).

[21] J. R. Ahn *et al.*, Mechanism of gap opening in a triple-band Peierls system: In atomic wires on Si, Phys. Rev. Lett. **93**, 106401 (2004).

[22] G. Kremer *et al.*, Direct observation of highly anisotropic electronic and optical nature in indium telluride, Phys. Rev. Mater. **7**, 074601 (2023).

[23] S. Misra *et al.*, Enhanced thermoelectric performance of InTe through Pb doping, J. Mater. Chem. C **9**, 14490 (2021).

[24] S. Misra *et al.*, Reduced phase space of heat-carrying acoustic phonons in single-crystalline InTe, Phys. Rev. Res. **2**, 043371 (2020).

[25] S. Y. Back *et al.*, Temperature-induced Lifshitz transition and charge density wave in $InTe_{1-\delta}$ thermoelectric materials, ACS Appl. Energy Mater. **3**, 3628 (2020).

[26] J. Zhang *et al.*, Direct observation of one-dimensional disordered diffusion channel in a chain-like thermoelectric with ultralow thermal conductivity, Nat. Commun. **12**, 6709 (2021).

[27] J. Zhang *et al.*, Dynamic lone pair expression as chemical bonding origin of giant phonon anharmonicity in thermoelectric InTe, Angew. Chemie- Int. Ed. **62**, e202218458 (2023).

[28] S. Pal and D. N. Bose, Characterisation and electrical anisotropy in layered chalcogenides gate and InTe, Solid State Commun. **97**, 725 (1996).

[29] M. Bouaziz *et al.*, Intrinsic defects and mid-gap states in quasi-one-dimensional indium telluride, Phys. Rev. Res. **5**, 033152 (2023).

[30] S. Luu *et al.*, Origin of low thermal conductivity in $In_4Se_3$, ACS Appl. Energy Mater. **3**, 12549 (2020).

[31] S. Fragkos *et al.*, Room temperature commensurate charge density wave in epitaxial strained $TiTe_2$ multilayer films, Adv. Mater. Interfaces **6**, 1801850 (2019).

[32] N. Zhou *et al.*, Low-symmetry 2D t-InTe for polarization-sensitive UV-Vis-NIR photodetection, Small 2400311 (2024).

[33] F. Bischoff *et al.*, Nanoscale phase engineering of niobium diselenide, Chem. Mater. **29**, 9907 (2017).

[34] G. Kremer *et al.*, Quantum confinement and electronic structure at the surface of van der Waals ferroelectric $\alpha$-$In_2Se_3$, ACS Nano **17**, 18924 (2023).

[35] A. Mahmoudi *et al.*, Quasi van der Waals epitaxy of rhombohedral-stacked bilayer $WSe_2$ on GaP(111) heterostructure, ACS Nano **17**, 21307 (2023).

[36] B. Hildebrand *et al.*, Short-range phase coherence and origin of the 1T-$TiSe_2$ charge density wave, Phys. Rev. B **93**, 125140 (2016).

[37] L. Khalil *et al.*, $\alpha$-As2Te3 as a platform for the exploration of the electronic band structure of single layer $\beta$-tellurene, Phys. Rev. B **106**, 125152 (2022).

[38] A. Erba *et al.*, CRYSTAL23: A program for computational solid state physics and chemistry, J. Chem. Theory Comput. **19**, 6891 (2023).

[39] J. Laun and T. Bredow, BSSE-corrected consistent Gaussian basis sets of triple-zeta valence with polarization quality of the fifth period for solid-state calculations, J. Comput. Chem. **43**, 839 (2022).

[40] F. Pascale, C. M. Zicovich-Wilson, F. L. Gejo, B. Civalleri, R. Orlando, R. Dovesi, The calculation of the vibrational frequencies of crystalline compounds and its implementation in the CRYSTAL code, J. Comput. Chem. **25**, 888 (2004).